Understanding the Ni migration in solid oxide cell: a coupled experimental and modeling approach

Léa Rorato, Yijing Shang, Shenglan Yang, Maxime Hubert, Karine Couturier, Lijun Zhang, Julien Vulliet, Ming Chen, Jérôme Laurencin

Understanding the Ni migration in Solid Oxide cell: a coupled experimental and modeling approach

Léa Rorato[(1)], Yijing Shang[(2)], Shenglan Yang[(2,3)], Maxime Hubert[(1)], Karine Couturier[(1)], Lijun Zhang[(3)], Julien Vulliet[(4)], Ming Chen[(2)], Jérôme Laurencin[(1)]

[(1)]Univ. Grenoble Alpes - CEA/LITEN, 38054, Grenoble, France
[(2)]Department of Energy Conversion and Storage, Technical University of Denmark, 2800 Kgs. Lyngby, Denmark
[(3)]State Key Laboratory of Powder Metallurgy, Central South University, Changsha 410083, China
[(4)]CEA, DAM, Le Ripault, F-37260, Monts, France

Abstract. A long-term test of 2000 h has been carried out on a typical solid oxide cell in electrolysis mode at -1 A.cm^{-2} and 750°C. The 3D reconstructions of the pristine and aged cermet have revealed a strong Ni depletion at the electrolyte interface. To explain this result, an electrochemical and phase-field model has been developed to simulate the Ni migration in Ni/YSZ electrode. For this purpose, a mechanism has been proposed that takes into account the impact of polarization on the Ni/YSZ wettability. In this approach, it assumes that the Ni/YSZ interfacial energy is changed by the concentration of oxygen vacancies in the electrochemical double layer. Thanks to the model, the Ni migration has been computed in the same condition than the experiment and complemented by a simulation in reverse condition in SOFC mode. In good agreement with the experiment, the simulations have revealed a strong Ni depletion at the electrolyte interface after operation under electrolysis current. On the contrary, a negligible Ni redistribution with a very slight Ni enrichment has been predicted at the electrolyte interface after SOFC operation. These results tend to prove the relevance of the mechanism.

Keywords. Solid Oxide Electrolysis Cell, Solid Oxide Fuel Cell, Ni migration, modeling, phase-field.

1. Introduction

Because of the global warming and the tremendous increase in the global energy demand, the massive use of renewable energy sources is becoming nowadays a priority. In this context, hydrogen is considered as an interesting energy vector that could be used in a climate-neutral society [1]. It has to be combined with an efficient electrochemical system able to produce electricity in fuel cell mode during the peaks of consumption and hydrogen in electrolysis mode during the low demand periods [2]. The high-temperature electrochemical device operating at 750°C-850°C is nowadays considered as one of the most promising technologies thanks to various advantages such as a high efficiency, a relative low cost and a good reversibility in fuel cell and electrolysis modes [3]. This technology is based on Solid Oxide Cells (SOCs) composed of a dense electrolyte usually in Yttria Stabilized Zirconia (YSZ) sandwiched between two porous electrodes. The hydrogen electrode is typically a cermet of Nickel and YSZ (Ni-YSZ) while the oxygen electrode is made of Mixed Ionic Electronic Conductors (MIEC) such as the Lanthanum doped-Strontium Cobalt Ferrite (LSCF) [3]. Despite all its advantages, the SOCs technology still faces some challenges to become economically competitive.

To date, the SOCs durability remains one of the main issue limiting the lifetime of this technology especially in electrolysis mode (SOEC). Indeed, the degradation rates in performances for the cells made of the state-of-the-art materials are less than around ≈ 1 %/kh in fuel cell mode (SOFC) whereas they can reach up to ≈ 2-3 %/kh when operated under electrolysis current [4] [5] [6]. The cell degradation is related to material instabilities, which are triggered by the high operating temperature and the polarization. They can have several origins, such as microstructural evolutions in the electrodes, active site poisoning, chemical-element interdiffusion and reactivity between the cell components [7] [8] [9] [10]. Specifically, the Ni particles in the cermet are not stable in operation and their rearrangement in the microstructure can affect significantly the cell response. Indeed, Ni particle coarsening is usually observed after operation in both SOFC and SOEC modes. It is due to the local agglomeration related to the growth of the biggest particles to the detriment of the smallest ones [11]. This phenomenon induces a decrease of the Triple Phase Boundary (TPB) lines, where the ionic, electronic and gas phases meet, decreasing the active sites for the electrochemical reactions [12]. Nevertheless, it has been shown that the Ni agglomeration

tends to slow down for long-term operation and can explain up to 25 - 30% of the total loss in performances [12] .

Aside from the local particle coarsening, Ni redistribution over long distance can also arise in the cermet. At very high temperature above 950°C, it has been shown that Ni can relocate at electrolyte interface in electrolysis mode [5]. However, a reverse trend is usually observed at the more classical SOC operating temperature below 900°C. Indeed, a substantial Ni migration away from the electrolyte interface is observed in electrolysis mode, even after a relative short-term operation [13]. For instance, Trini et al. [14] and Monaco et al. [15] have both detected a fully depleted layer of Ni at the electrolyte interface for cells operated at 800°C for 1000 h. On the contrary, as reported by Menzler et al. [16], a slight Ni enrichment can occur in fuel cell mode, which was only detected after a very long-term operation of 100,000 h at 700°C. It can be noticed that the Ni depletion in SOEC operation is also concomitant with some detachments of Ni from YSZ [17]. Moreover, it has been shown that the cermet microstructure plays a key role on the Ni migration. Indeed, finer microstructure in the active layer seems to mitigate in part the Ni redistribution [18]. In electrolysis mode, the depleted layer of Ni in the vicinity of the electrolyte interface is responsible of a noticeable increase in the Ohmic cell resistance [19]. The Ni migration also leads to gradient of TPB in the depth of the electrode that increases the cell polarization resistance [15]. Therefore, the Ni migration in electrolysis mode is considered as one of the most detrimental phenomena that must partially explain the difference in durability behavior between SOFC and SOEC modes.

Even if the underlying mechanisms involved in the Ni migration are still not precisely understood, different scenarios have been already reported in the literature. Mogensen et al. [13] [20] have proposed a mechanism based on the Ni particles detachment from YSZ as well as the loss of contact between Ni particles due to their coarsening. Indeed, these particles, which are not polarized anymore, can diffuse under Ni(OH)x species towards (resp. away from) the electrolyte in SOFC mode (resp. SOEC mode). The Ni(OH)x species can diffuse either in the gas phase at high temperature (900°C) or on the surface at lower temperature (800°C). When the mechanism is controlled by surface diffusion, Trini et al. [14] have suggested that Ni migration could be driven by the gradient in oxygen partial pressures associated to the local electrode polarizations arising in the electrode thickness. This gradient induces a variation of Ni wettability on YSZ depending on the position in the electrode. In electrolysis mode, the low wettability of Ni onto YSZ at the electrolyte interface induces a Ni migration towards the bulk of the electrode. The reverse gradient arising in fuel cell mode

must account for the Ni relocation at the electrolyte interface. Nevertheless, in spite of the lower anodic polarizations with respect to the cathodic ones [14], this mechanism should lead to significant Ni migration towards the electrolyte interface in fuel cell mode, which is not experimentally observed [16]. Moreover, the wettability gradients calculated in SOEC mode with this hypothesis are insufficient to account for a substantial Ni depletion [21]. In that condition, this mechanism based on the Ni surface tension seems not to play a major role on the Ni redistribution in porous electrode microstructure. In parallel, Nakajo et al. [22] have suggested that the mechanism could be related to an electrocapillarity phenomenon [23]. In this pure thermodynamic approach, the Ni/YSZ interfacial energy must be also affected by the electrode potential. Nevertheless, according to the Young–Lippmann equation, the Ni wettability onto YSZ should increase at high polarization in both electrolysis and fuel cell modes. In other words, as mentioned in [20], the effect of polarization must 'result in a fairly symmetrical decrease of the interfacial energy around the electrocapillary maximum'. This evolution seems to be contradictory with the observations and cannot explain the Ni redistribution in both operating modes. Finally, Monaco et al. [15] have suggested that the mechanism could be linked to the accumulation of charges in the electrochemical double layer at the Ni/YSZ interface. In SOEC mode, the strong accumulation of oxygen vacancies in the YSZ at the Ni/YSZ interface could decrease the Ni wettability onto YSZ. Conversely, the depletion of vacancies in SOFC mode should not affect significantly the wettability. It can be noticed that the decrease of the work of adhesion in electrolysis mode could also explain the Ni detachment observed after operation. Despite their differences, it is worth noting that all the mechanisms assume that the gradient in local polarization across the electrode controls the Ni migration.

The modeling can be an efficient tool to unravel the complex and entangled phenomena involved in the Ni microstructural evolutions in the cermet. Many models have been already proposed to simulate accurately the Ni coarsening. Semi-phenomenological approaches such as power-law models have been used to calculate the growth of the mean Ni particle diameter over the time [12]. More sophisticated models have been also developed thanks to a detailed mechanistic description of the Ni coarsening phenomenon [24]. In this frame, the phase-field method has been successfully applied to reproduce accurately the Ni agglomeration in the 3D microstructure [25] [26] [27]. To the best of our knowledge, only few models was dedicated to simulate the Ni migration using the phase-field approach [28] [29]. In the work of [28], the model was based on the mechanism proposed by Trini et al. [14] while the electrode

overpotentials were estimated using a Butler-Volmer expression for the electrochemical reaction at TPB. The authors have successfully simulated the Ni depletion in SOEC mode proving the relevance of the phase-field method to simulate the Ni migration. Whatever the envisaged mechanism for Ni migration, it is worth noting that the phase-field simulations should be coupled to an electrochemical model able to predict correctly the dissymmetry of the electrode polarization curve in SOFC and SOEC modes [30]. Even if the precise mechanism for the electrochemistry at the surface of Ni and YSZ is still a subject of investigation, it has been shown that a decomposition of the reaction pathways in elementary steps can provide satisfactory description of the electrode response [30]. More specifically, it has been found that the elementary model developed in [30], which is based on a hydrogen spillover mechanism, is able to capture the dissymmetry of the electrode polarization in SOFC and SOEC modes depending on the hydrogen and steam partial pressures.

In this work, a mechanism based on the approach of Monaco et al. [15] is proposed to account for the Ni migration in both fuel cell and electrolysis modes. This model combines the evolutions of the electrochemical double layer and the Ni wettability on YSZ depending on the polarization. To illustrate the relevance of this mechanism, the Ni migration is simulated in fuel cell and electrolysis modes coupling the phase-field method to a multi-scale electrochemical model. The simulated results are discussed and compared to experimental data obtained for a specific long-term test performed in electrolysis mode at high current density.

2. Experiments and models

2.1 Cell description

A hydrogen electrode supported cell manufactured by CEA was used for the experiments. The cell has a circular shape with an active area of 9.08 cm^2. The cell is composed of a thick cermet substrate of 280 µm made of NiO and zirconia stabilized with 3 mol.% of yttria (NiO-3YSZ) on which is deposited a functional layer of 25 µm in NiO and zirconia stabilized with 8 mol.% yttria (NiO-8YSZ). The Ni-to-YSZ weight ratios for the active layer and the support are respectively, 8YSZ/Ni=46 wt% / 54 wt% and 3YSZ/Ni=56 wt% / 44 wt%. The dense and thin electrolyte of 8 µm, which consists of 8YSZ, was co-sintered with the cermet support. The oxygen electrode deposited by screen-printing onto the electrolyte has a bilayer structure. The active part of the oxygen electrode is a 22 µm thick porous layer constituted of a LSCF-

CGO composite with $La_{0.6}Sr_{0.4}Co_{0.2}Fe_{0.8}O_{3-\delta}$ (LSCF) perovskite and 20 mol.% Ceria doped Gadolinium Oxide (CGO). The current collector is made of LSCF with a thickness of 20 µm. A thin barrier layer of CGO (ca. 3 µm thick) is added between the electrolyte and the oxygen electrode to avoid the formation of secondary insulating phases.

Regarding the fabrication of the Ni-8YSZ functional layer, submicronic powders were obtained with a particle size distribution ranging from 0.5 µm to 1 µm after a ball milling step performed on the initial powders. A classical organic solvent was used as ink vehicle to prepare paste. The powders and the binder were mixed together before passing through a tricylinder grinder. The paste was then deposited on the NiO-8YSZ support by screen-printing using a grid with a standard mesh size. The layer was finally sintered under air at high temperature (above 1400 °C). It can be noticed that a similar procedure was applied to deposit the barrier layer and the LSCF-CGO functional layer sintered under air above 1200 °C and below 1100 °C, respectively.

2.2 Electrochemical set-up and test conditions

A durability test was performed in a test bench developed for operation in fuel cell and electrolysis modes. The cell holder at the hydrogen side is made of Crofer 22 APU while an alumina diffuser is used at oxygen side (Fig. 1). For each electrode, the gases are introduced at the cell center with a radial co-flow configuration. Brooks SLA5850S mass flow controllers assume the delivery of the gases (Air, N_2, H_2 and steam produced from deionized water in a homemade evaporator). The precision of the steam mass flow meter after its calibration is +/- 0.09 NL/h (which is rather negligible compared to the inlet steam flow rate of 5.8 NL/h). Moreover, in order to check the actual steam content sent to the cell, the steam at the cell outlet was weighed after its condensation. It can be noticed that a reasonable agreement was obtained between the mass flow controller set point and the weight of water measured at the cell outlet (with an error of less than 10%). As depicted in Fig. 1, a glass ceramic Schott G018-311 seal is deposited at the cell periphery to ensure the gas tightness of the hydrogen compartment. Nickel and gold grids are used for the current collection at the hydrogen and oxygen sides, respectively. A load of 600 $g.cm^{-2}$ is added on the top of the set-up to minimize the contact resistances between the electrodes and the grids.

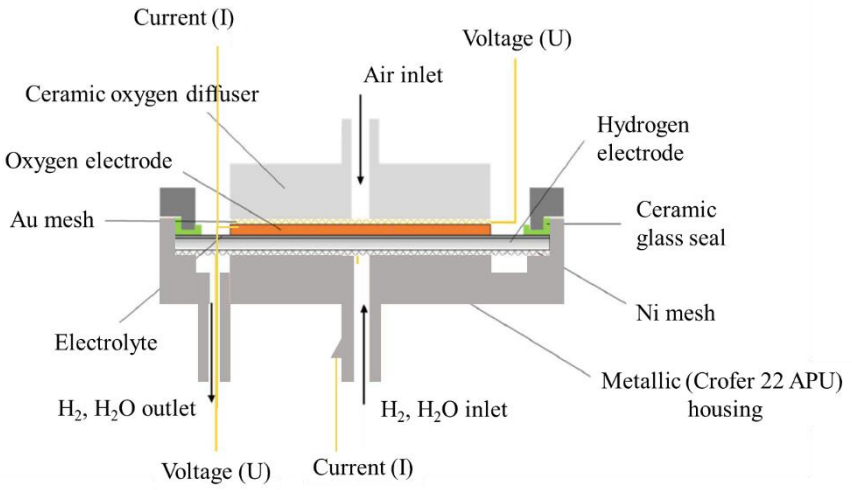

Figure 1: Schematic representation of the experimental set-up for the durability experiment.

For the experiment, the cell was heated-up at 1 °C.min^{-1} by feeding respectively the oxygen and hydrogen compartments with air and nitrogen. After a thermal treatment at temperature higher than 800°C for the formation of the glass seal, the temperature was stabilized at 800°C for the cermet reduction carried out by introducing progressively hydrogen into nitrogen. After the complete reduction of NiO into Ni, the temperature was lowered to 750°C and initial electrochemical characterizations including polarization curves and Electrochemical Impedance Spectroscopy (EIS) diagrams were recorded before starting the durability experiments. The long-term test in electrolysis mode was performed for 2000 h at 750°C in galvanostatic mode at -1 A.cm^{-2} with a Steam Conversion (SC) of 64% and a gas composition of 90%vol. H_2O and 10%vol. H_2. The cell voltage was continuously monitored during the test while intermediate EIS diagrams at Open Circuit Voltage (OCV) were acquired at 400, 1000, 1600 and 2000 h. Finally, a polarization curve was measured at the end of the experiment. The cell was then cooled down at room temperature by sweeping the Ni-YSZ electrode under hydrogen. A second cell was reduced in the same set-up and used as a reference for the study. All the electrochemical characterizations were conducted using a potentiostat/galvanostat (Autolab PGSTAT-302N) equipped with a Frequency Response Analyzer module (FRA) and a 20 A current booster.

2.3 Microstructural characterizations

2.3.1 SEM observations – Polished cross-sections of the reference and aged cells were observed using a Field Emission Gun - Scanning Electron Microscope (FEG-SEM, ZEISS Merlin). Before the observations, the cells were cut and embedded in an epoxy resin

(Epofix®) under vacuum to fill the open porosity. Then, the cross-sections were polished step by step until a final stage using silica spray of 0.03 µm. A thin carbon layer was finally deposited on the surface to avoid charging artefacts during the observations. The SEM images were obtained in Back-Scattered Electrons (BSE) mode with an acceleration voltage of 2 kV and a working distance of 5 mm.

2.3.2 FIB-SEM reconstructions – The reference and the aged electrode microstructures have been reconstructed using a Focused Ion Beam - Scanning Electron Microscope (FIB-SEM, Zeiss CB550). SEM images were acquired using Energy Selective Back-Scattered (ESB) and standard Secondary Electron (SE) detectors, with a voltage of 1.5 kV and a pixel size of 10 nm. FIB milling between two successive slices was also taken to 10 nm in such a way that the voxel size in the reconstruction is 10^3 nm^3. Acquired volumes are a few tenth of microns large in each direction. After acquisition and image processing to align and correct artifacts, a segmentation by machine-learning was done using Ilastik software [31] [32].

2.4 Models

2.4.1 Multiscale electrochemical model – A multi-scale electrochemical model has been used in this study to assess the local electrode polarization in the cermet. This model has been already detailed in [33] and is briefly described hereafter. It combines two micro-scale electrode models to a macroscopic description including the cell geometry and the radial co-flow configuration of the test bench (cf. Fig. 1). At the macroscopic scale, the model is able to compute the distribution of molar fractions along the gas channel and within the porous electrodes [33] . The repartition of the electrode overpotentials together with the Ohmic losses is also a model output. In this multiscale approach, the partial pressures calculated at the macroscopic scale are used as boundary conditions at the top of the active layer for the electrode models. These microscale models are used to calculate the electrode polarization or activation overpotentials along the cell length thanks to an elementary description of the reaction pathways. The elementary model for the oxygen electrode active layer made of LSCF-CGO is extensively detailed in [34] and is validated in both SOEC and SOFC modes. The thorough description of the elementary kinetic model for the Ni-YSZ hydrogen electrode can be found in [30]. The model is based on a hydrogen spillover mechanism taking into account gas interactions with both Ni and YSZ surfaces. This model is able to predict accurately the dissymmetry of the electrode polarization in SOFC and SOEC modes. It is worth noting that the integrated model combining the different length-scales has been specifically validated for the studied cell as detailed in [33]. In the present work, the model

has been used to compute the cell polarization curve and the impedance spectra at OCV as well as the local electrode polarization in the hydrogen electrode.

2.4.2 Phase-field modeling for microstructural evolution – The phase-field method has emerged as a powerful tool to simulate microstructure evolution based on the minimization of the free energy. Based on the phase-field method, Steinbach et.al. have proposed a multi-phase-field (MPF) model to quantitatively simulate the microstructure evolution of multi-component and multi-phase systems during various materials service processes [35] [36] [37] [38]. In MPF, input of reliable thermo-physical parameters (such as interface energy and diffusion coefficient) and key experimental validation are essential to achieve quantitative simulation results. Besides, using experimental microstructure as initial inputs is another key point for performing quantitative simulations.

In this work, the MPF model has been adapted to the Ni-YSZ system composed of three phases, i.e. the gas phase (porosity), the oxygen ion (YSZ) and electronic (Ni) conducting phases. Since YSZ is rather stable during long-term operation, neither phase transformation in YSZ nor chemical reaction with Ni have been assumed in this study. For the Ni-YSZ cermet, the total free energy functional, which consists of interfacial energy and chemical energy, can be formulated as follows [38]:

$$F = \int_{\Omega} f^{intf} + f^{chem} \tag{1}$$

$$f^{intf} = \sum_{\alpha,\beta=\mathrm{Pore,YSZ,Ni},\alpha\neq\beta} \frac{4\sigma_{\alpha\beta}}{\eta_{\alpha\beta}} \left\{ -\frac{\eta_{\alpha\beta}^2}{\pi^2} \nabla\phi_\alpha \cdot \nabla\phi_\beta + \phi_\alpha\phi_\beta \right\} \tag{2}$$

$$f^{chem} = \sum_{\alpha=\mathrm{Pore,YSZ,Ni}} \phi_\alpha f_\alpha\,(c_\alpha) + \tilde{\mu}\left(c - \sum_{\alpha=Pore,YSZ,Ni} \phi_\alpha c_\alpha \right) \tag{3}$$

where ϕ_α is the phase field variable of the α phase which satisfies the sum constraint $\sum_{\alpha=\mathrm{Pore,YSZ,Ni}} \phi_\alpha = 1$. The term $\sigma_{\alpha\beta}$ is the interfacial energy between the α and β phases while $\eta_{\alpha\beta}$ is the phase-field interfacial width. $f_\alpha(c_\alpha)$ is the bulk free energy density of the individual phase depending on the phase concentrations c_α. It can be derived from the CALPHAD thermodynamic database. $\tilde{\mu}$ is the diffusion potential of component Ni introduced as a Lagrange multiplier to conserve the mass balance between the phases $c = \sum_{\alpha=\mathrm{Pore,YSZ,Ni}} \phi_\alpha c_\alpha$.

Considering that the system always moves towards the free energy minimum, the MPF evolution equations can be expressed as a function of the interface mobility and free energy. Through the antisymmetric approximation of the MPF evolution equations, the time derivative of the phase-field variable for each phase can be written as follows [35]:

$$\dot{\phi}_\alpha = \sum_{\alpha,\beta=\mathrm{Pore,YSZ,Ni}} \mu_{\alpha\beta}\left\{\sigma_{\alpha\beta}\left[\phi_\beta\nabla^2\phi_\alpha - \phi_\alpha\nabla^2\phi_\beta + \frac{\pi^2}{2\eta^2}\left(\phi_\alpha - \phi_\beta\right)\right] + \frac{\pi}{\eta}\sqrt{\phi_\alpha\phi_\beta}\Delta g_{\alpha\beta}\right\} \quad (4)$$

where $\mu_{\alpha\beta}$ is the interface mobility between α and β phases. $\Delta g_{\alpha\beta}$ is the local deviation from thermodynamic equilibrium and given as [38]:

$$\Delta g_{\alpha\beta} = -f_\alpha(c_\alpha) + f_\beta\left(c_\beta\right) + \tilde{\mu}\left(c_\alpha - c_\beta\right) \quad (5)$$

For a multicomponent system, a set of diffusion equations for all solute components, which are generally not independent but linked by cross terms, is required. These equations are derived for the conserved compositions c_α from the free energy functional by a relaxation approach. Considering the constraint of quasi-equilibrium [38] and following the example of a ternary system by Wu [39], the equations for the Ni/YSZ system can be written as:

$$\dot{c} = \nabla \sum_{\alpha=\mathrm{Pore,YSZ,Ni}} \phi_\alpha D_\alpha \nabla c_\alpha \quad (6)$$

where D_α is the chemical diffusion coefficient matrix. The detail on phase field modelling of the Ni/YSZ electrode microstructure evolution using the MPF method will be reported elsewhere.

In the present work, the MPF simulations have been carried out using the FIB-SEM 3D reconstruction of the tested electrode as initial microstructure. In the model, both Ni surface and bulk diffusions cannot be separated. They are taken into account in an effective coefficient calibrated thanks to in-situ characterization of 3D Ni/YSZ microstructure [37]. The calibrated value, $D_{Ni} = 3.5 \times 10^{-14}\mathrm{m}^2.\mathrm{s}^{-1}$, is thus between the bulk diffusivity and surface diffusivity reported in literature.

Compared to Ni, the diffusion coefficient of YSZ can be neglected [40]. Therefore, the YSZ diffusion coefficient was set to zero in the phase field simulation. The gradients through the electrode thickness in Ni/YSZ interfacial energy σ_{Ni-YSZ} (related to the Ni wettability on YSZ through the classical Young-Dupré equation) were calculated with the electrochemical model

(cf. section 4.2.2) while the Ni/pore and YSZ/pore interfacial energies are equal to $\sigma_{Ni-pore} = 0.23\ \mathrm{J\ m^{-2}}$ and $\sigma_{YSZ-pore} = 0.18\ \mathrm{J\ m^{-2}}$ [41].

3. Experimental results

3.1 Cell performances and degradation

The initial polarization curves measured for three inlet gas fluxes at 750°C are shown in Fig. 2a. Good performances are achieved at the thermo-neutral voltage (1.3 V) with current densities reaching –0.72 A.cm^{-2}, –0.94 A.cm^{-2} and -1 A.cm^{-2} for steam conversion of 84% (i.e. for an inlet steam flow rate of 6 Nml.min^{-1}.cm^{-2}), 75% (i.e. 9 Nml.min^{-1}.cm^{-2}) and 64% (i.e. 12 Nml.min^{-1}.cm^{-2}), respectively. The polarization curves measured at 750°C on three different cells are shown in Fig. 2b. A very good reproducibility has been found suggesting that the electrode microstructures of the tested cells are well comparable.

A typical impedance diagram recorded at OCV is shown in Fig. 2c. The diagram presents three arcs at low, intermediate and high frequencies. The contribution at high frequency is distorted by an inductance related to the set-up wires. To correct the artefact introduced by this inductive effect, the diagram has been fitted using a classical Equivalent Circuit (EC) as proposed in [42] [43]. As depicted in Fig. 2d, this EC model is composed of (i) an inductance (L) taking into account the contribution of the wires, (ii) a resistance (R_{ohm}) associated to the pure Ohmic losses, (iii) two resistance-capacitance elements (R-C) representative of the high frequency contribution, and (iv) two resistance-constant phase element groups (R-CPE) related to the medium and low frequencies arcs. After fitting, the EC model was used without the inductance to simulate a second diagram corrected from the effect of the wires (Fig. 2c). As expected, the series resistance in the simulated spectrum is decreased compared to the initial diagram while the high frequency contribution is enlarged (Fig. 2c).

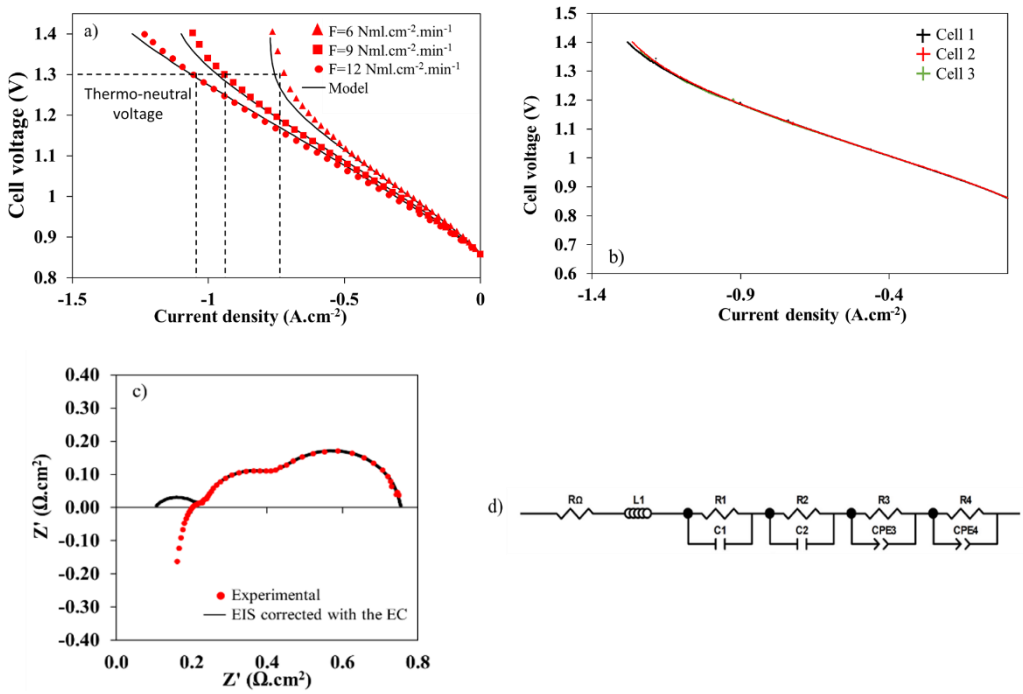

Figure 2: a) Initial experimental and simulated polarization curves measured at 750°C, pH_2/pH_2O = 0.1/0.9 and 6, 9 and 12 Nml.cm^{-2}.min^{-1} b) Initial iV curves at 750°C, pH_2/pH_2O = 0.1/0.9, 12 Nml.cm^{-2}.min^{-1} measured on three different cells, c) Experimental EIS and after its correction using the EC (OCV at 750°C, pH_2/pH_2O = 0.1/0.9 and 6 Nml.cm^{-2}.min^{-1}) and d) Equivalent circuit model used to analyze the EIS spectra obtained at 750°C and pH_2/pH_2O = 0.1/0.9.

The durability curve, which was carried out at 750°C and -1 A.cm^{-2}, reveals a significant increase of the cell voltage over the time (Fig. 3a). After a short transient period of ≈ 70 h, the curve exhibits three main parts from (i) 220 h to 400 h, (ii) 500 h to 800 h and (iii) 1100 h to the end of the test (marked I, II and III in Fig. 3a). The degradation rates for these three periods are respectively (i) 139 mV/kh (≈ 11 %/kh), (ii) 218 mV/kh (≈ 17 %/kh) and (iii) 45 mV/kh (≈ 3 %/kh). It can be noticed that, after the first and second periods, the degradation rate tends to stabilize towards a constant value which is consistent with the data reported in the literature [44]. EIS diagrams have been acquired during the durability test under polarization at i_{DC} = -0.2 A.cm^{-2}. The diagrams are shown in Fig. 3b after correction of the inductive artefact according to the aforementioned procedure. Their analysis as a function of time reveals a substantial increase of both the series resistance and the high frequencies arc whereas the low and medium contributions remain almost unchanged. Indeed, the Ohmic

resistance is increased from 0.164 Ω.cm^2 to 0.213 Ω.cm^2 while the resistance of the high frequency arc is increased from 0.055 Ω.cm^2 to 0.117 Ω.cm^2.

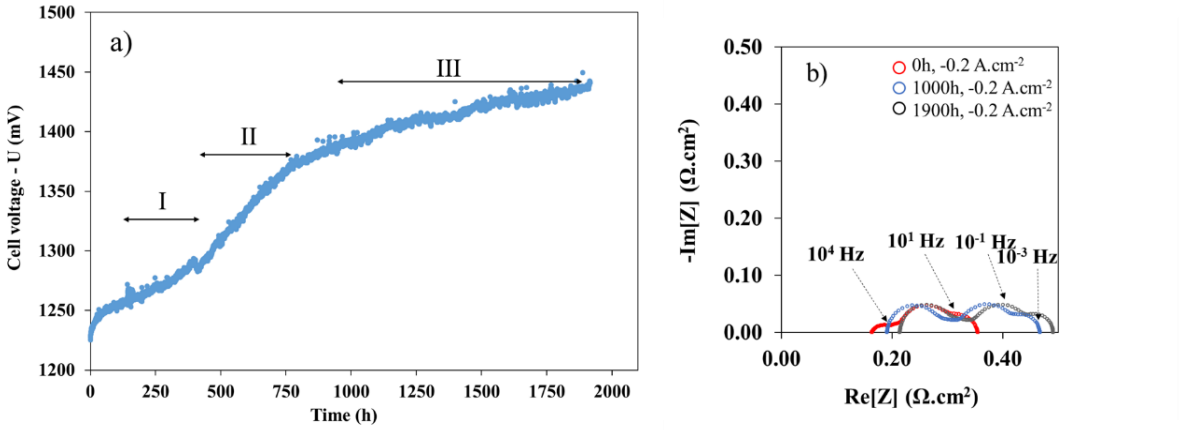

Figure 3: a) Durability curve (cell voltage as a function of time) at 750°C, in electrolysis mode, -1 A.cm^{-2}, pH_2/pH_2O = 0.1/0.9, 12 Nml.cm^{-2}.min^{-1} and SC = 64% and b) EIS measured under polarization (i_{dc}=-0.2 A.cm^{-2}) at 0h, 1000h and 1900h (750°C, pH_2/pH_2O = 0.1/0.9 and 12 Nml.cm^{-2}.min^{-1}). The diagrams have been corrected of the wires inductance using EC showed in Fig. 2d.

3.2 Microstructural evolution

3.2.1 SEM electrode observations – The SEM images of the Ni-8YSZ functional layer are shown in Fig. 4 for both the reference and the aged cells. It can be observed that the pristine cermet presents a homogeneous and rather fine microstructure (Fig. 4a). On the contrary, agglomeration of some Ni particles are detected in the aged cermet (Fig. 4b). Besides, a strong migration of Ni away from the electrolyte interface is observed in the micrographs after operation (Fig. 4b and 4c). Finally, a detachment of the remaining Ni particles all along the electrolyte interface has been also observed as shown in Fig. 4c. These results are consistent with previous observations reported in the literature for cell aged in electrolysis mode [15].

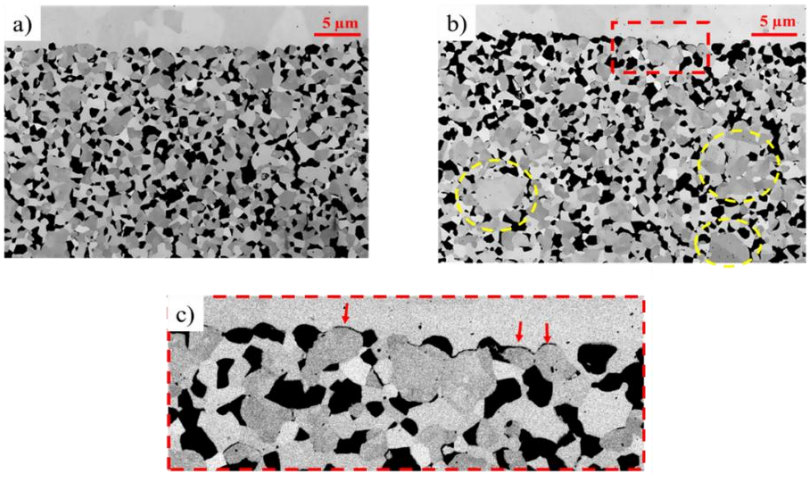

Figure 4: SEM images of the electrolyte/electrode interface for: a) the reference cell, b) the cell operated 2000 h in electrolysis mode (agglomeration is shown by the yellow dotted line) and c) zoom at the electrolyte interface of the aged cell (porosity = black, YSZ = white, Ni = grey).

3.2.2 Reconstruction for the reference and the aged electrode (active layer) – The FIB-SEM 3D reconstructions have been extracted at ≈1 cm away from the cell center in such way that the local current density is close to -1 A/cm² (cf. Fig. 8a). The 3D rendering volumes for the reference and the aged cells are presented in Fig. 5a and b respectively. In agreement with the SEM characterizations, the visual inspection of both volumes confirms the strong microstructural evolution after ageing in electrolysis mode. Indeed, a substantial Ni agglomeration and migration away from the electrolyte interface is observed.

In complementary with the observations, sub-volumes of 18 × 19 × 23 = 7866 µm^3 for the reference cell and 27 × 7.8 × 25 = 5265 µm^3 for the aged one have been extracted from the whole reconstructions to calculate the microstructural properties of the percolated phases. It is worth noting that these sub-volumes are substantially higher than the Representative Volume Element (RVE) of 12×12×12=1728 µm^3 for this type of cermet microstructure that allows getting good statistics on the properties [45].

The microstructural properties of the cermet were computed from the segmented sub-volumes thanks a set of numerical tools already detailed in [46] [45]. The overall volume fractions of pore, Ni and YSZ for the pristine cell (respectively 0.247, 0.383 and 0.37) have been found to be very similar to the ones obtained after ageing (respectively 0.244, 0.386 and 0.37). As expected, the computation has revealed that the mean diameter of the Ni particles has increased from 0.57 µm to 0.67 µm due to Ni coarsening. Moreover, the active TPB density

and the specific surface area between Pore and Ni have decreased from 2.85 μm^{-2} to 2.57 μm^{-2} and from 0.61 μm^{-1} to 0.402 μm^{-1} respectively.

To highlight the Ni migration, the evolution of the phase volume fractions and active TPB density has been calculated as a function of the position in the electrode thickness according to the method reported in [15]. As expected, it is found that the YSZ phase is not changed after operation [47] whereas the loss of Ni takes place over a distance of $\approx$ 4 µm from the electrolyte interface. This evolution is associated to an increase in the pore volume fraction leading to a significant decrease in the density of active TPB that must explain the cell degradation in performances. The mass centers for the pore and Ni phases have been also calculated on the reconstructions over a distance of 23 µm away the electrolyte interface. The mass center for the pores has moved from 11.65 µm to 10.57 µm toward the electrolyte whereas the Ni one has moved from 11.99 µm to 12.61 µm away from the electrolyte. This result confirms the substantial Ni migration after ageing in electrolysis mode.

The local heterogeneities in the two microstructures can induce an uncertainty in the estimation of the local properties as a function of the position in the electrode thickness. For instance, the average for the YSZ volume fraction measured over the distance between 14 and 20 microns away from the electrolyte decreased from ≈0.39 for the reference up to ≈0.34 for the aged cell (Fig. 5c). Since the YSZ backbone must remain unaffected by the ageing, it can be proposed that the uncertainty due to these local heterogeneities can reach up to 12% for the volume fractions. At 2 µm from the electrolyte interface, the Ni volume fraction decreases from ≈0.42 down to ≈0.21 (i.e. a decrease of 50%). This evolution related to the Ni depletion is thus significantly higher than the uncertainty.

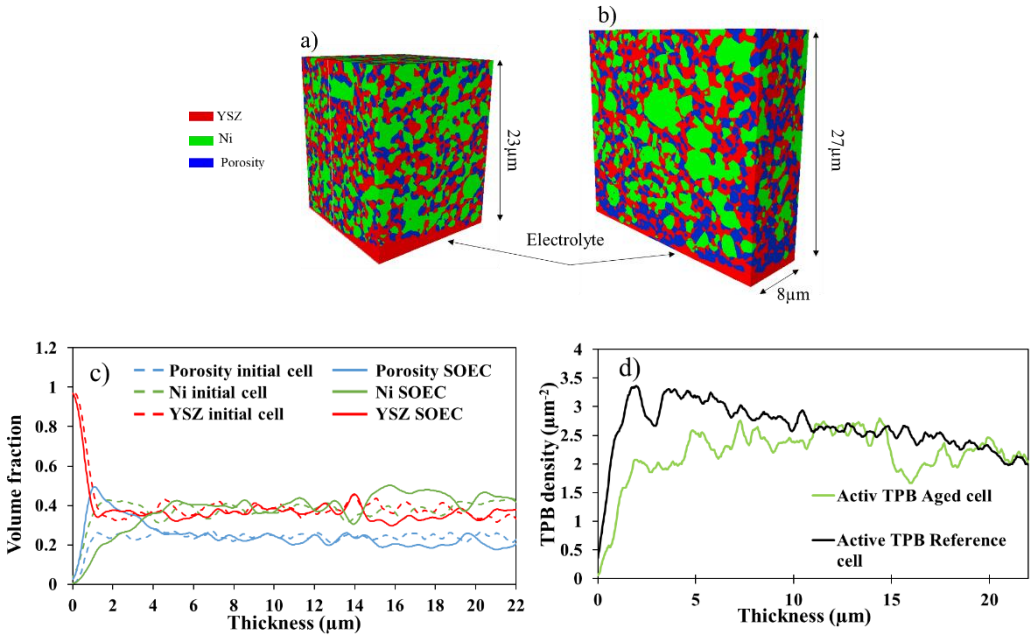

Figure 5: FIB-SEM reconstructions for: a) the reference and b) cell operated 2000 h in electrolysis mode containing a part of the Ni-YSZ electrode and a part of the electrolyte, c) profiles of the phase volume fractions of the Ni, the YSZ and the pore phases for the initial and aged cells and d) profiles of the active TPB density for the reference and the aged cells.

4. Modeling results and discussion

4.1 Description of the proposed mechanism

The proposed mechanism to account for the Ni migration is based on a change of the Ni/YSZ interface chemistry under polarization. Indeed, the oxygen vacancies concentration in the electrochemical double layer can be significantly affected by the local electrode overpotential. If considering a blocking electrode, which is well representative of the bulk of the Ni/YSZ interface away from the TPBs lines (where there is no electrochemical reaction), the concentration of vacancies in the vicinity of the Ni/YSZ interface can be estimated as a function of the position in the electrode *(r,z)* through the local overpotential $\eta\,(r,z)$ [48]:

$$C_{V\ddot{o}}^{int}(r,z) = \frac{C_{V\ddot{o}}^{max} C_{V\ddot{o}}^{bulk} \exp\left(-\frac{2F}{RT}\eta(r,z)\right)}{C_{V\ddot{o}}^{max} + C_{V\ddot{o}}^{bulk}\left(\exp\left(-\frac{2F}{RT}\eta(r,z)\right) - 1\right)} \quad (7)$$

where $C_{V\ddot{o}}^{int}$, $C_{V\ddot{o}}^{max}$ and $C_{V\ddot{o}}^{bulk}$ denote respectively the oxygen vacancy concentration at the Ni/YSZ interface, the maximum and the bulk concentrations in YSZ. The term $C_{V\ddot{o}}^{bulk}$ is

expressed as a function of the molar percentage of Yttria in 8YSZ, i.e. $\%Y_2O_3 = 0.08$, the volume of the unit cell V_{uc} for cubic zirconia and the Avogadro's number Na:

$$C_{V_{\ddot{O}}}^{bulk} = 4 \cdot \frac{\%Y_2O_3}{V_{uc} \cdot Na} \quad (8)$$

In the model, it is assumed that the maximum concentration $C_{V_{\ddot{O}}}^{max}$ of vacancies in the double layer is reached when all the oxygen atoms have been removed from YSZ:

$$C_{V_{\ddot{O}}}^{max} = \frac{8}{V_{uc} \cdot Na} \quad (9)$$

For a radial position *r* along the cell radius (cf. Fig. 6), the local overpotentials must present a steep gradient in the depth of the electrode *z* with higher absolute value at the electrolyte interface ($z = 0$) than the top of the active layer (z = ℓ): $|\eta_{act}(r, z = 0)| > |\eta_{act}(r, z = \ell)|$ (cf. system of coordinates in Fig. 6). It can be noted that, for a given current density, a higher gradient in local electrode overpotentials is expected in SOEC mode with respect to the SOFC one (because of the dissymmetry of the electrode polarization curve [49]). According to eq. (7), these gradients will induce a variation in oxygen vacancies concentration in the double layer as a function of the electrode thickness. As depicted in Fig. 6, a strong accumulation of oxygen vacancies in the double layer should appear at the electrolyte interface ($z = 0$) in SOEC mode while a moderate depletion is expected in SOFC mode.

The oxygen vacancies in the double layer are liable to affect significantly the adhesion between both materials and hence the wettability of Ni onto YSZ (which is the ability of the Ni to maintain contact with the YSZ surface). Indeed, the Ni/YSZ adhesion is mainly ensured by the Ni-O bonds at the interface between the metal and the ceramic [50]. Therefore, the modification of the oxygen vacancies concentration in the double layer under polarization will change the number of bonds at the interface. Under cathodic polarization, the interface must be weakened since the oxygen atoms participating to the adhesion are replaced by the oxygen vacancies accumulated in the double layer. Because of the gradient in overpotentials (and hence in oxygen vacancies), the Ni adhesion onto YSZ must be preferentially lowered at the electrolyte interface ($z = 0$). As a consequence, a gradient in Ni/YSZ contact angle related the Ni wettability onto YSZ should arise in the electrode thickness with higher values at the electrolyte interface than in the bulk as illustrated in Fig. 6. This gradient could constitute the driving force for the Ni migration away from the electrolyte interface in SOEC mode. Conversely, the Ni/YSZ interface must be strengthened under anodic polarization by the depletion of vacancies in the double layer. In other words, the adhesion should be enhanced

especially at the electrolyte interface. Accordingly, a wettability gradient should appear in the electrode thickness with a lower Ni/YSZ contact angle at the electrolyte interface (Fig. 6). These gradients could thus explain the Ni enrichment at the electrolyte interface observed after SOFC operation. It is worth noting that the strong accumulation of vacancies and the steep gradients under cathodic polarizations would trigger a rapid depletion as experimentally observed while the lower gradients in SOFC mode should be consistent with the slow Ni enrichment at the electrolyte interface. To better illustrate the validity of this mechanism, a quantitative modeling is proposed in the next section.

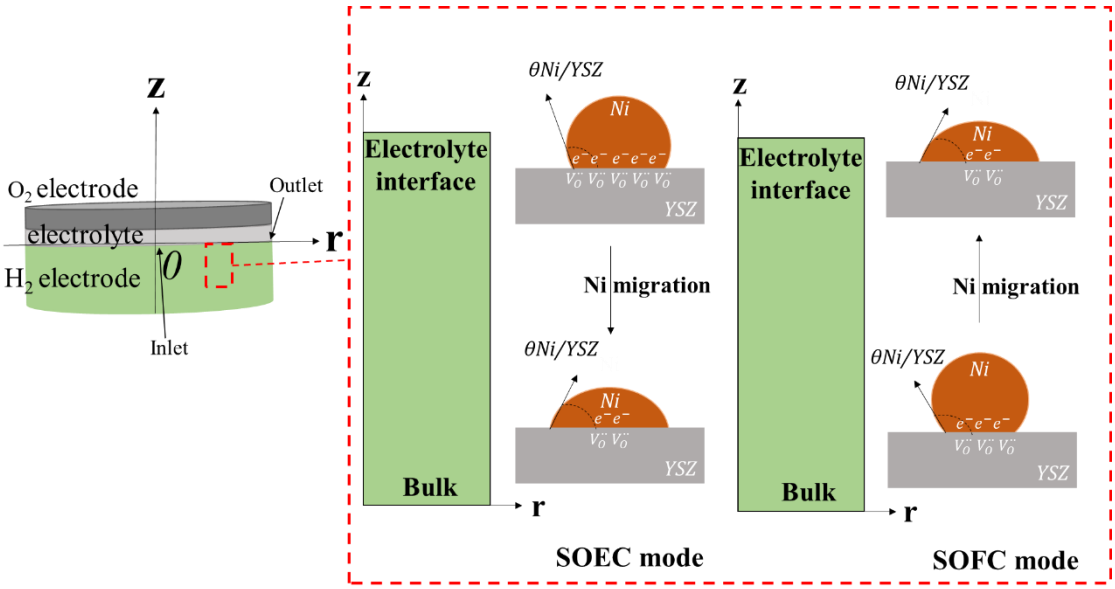

Figure 6: Schematic representation of the Ni migration mechanism in both SOFC and SOEC modes with the system of coordinates used for the modeling.

4.2 Simulations for the Ni migration in SOEC and SOFC modes

4.2.1 Electrochemical simulations – The simulated polarization curves are compared to the experimental data at 750°C in Fig. 2a. A general good agreement is found for the three presented cases. More specifically, the model is able to capture correctly the limiting current density at high steam conversion. A good match is also found between the simulated and the experimental impedance spectra as shown in Fig. 7. As discussed in [33], the shape of the impedance in the Nyquist plot as well as the frequency distribution in the Bode plan are rather well reproduced by the physically-based model. Thanks to the simulations, the three contributions in the impedance spectra can be identified unambiguously. It has been found that the low frequency arc is mainly related to the gas conversion and diffusion in the cermet support. The contribution at medium frequencies is associated to the electrochemical and

transport processes in the active layer of the oxygen electrode. The contribution at high frequencies is mainly related to the processes in the hydrogen electrode [33].

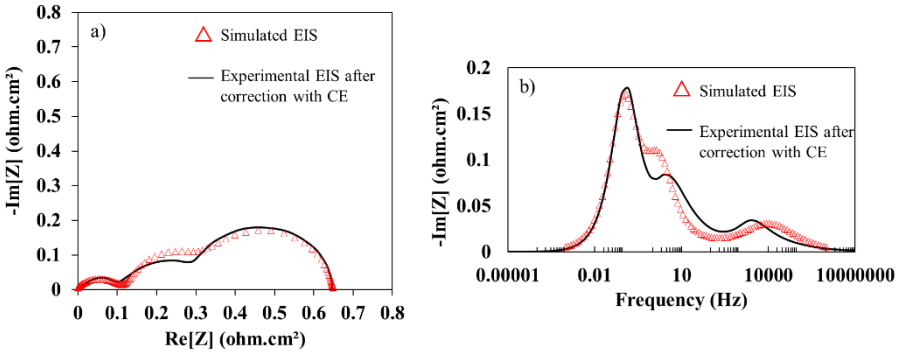

Figure 7 a) Simulated Nyquist plot and experimental one after correction with the CE at OCV, at 750°C, pH_2/pH_2O = 0.1/0.9 and 6 Nml.cm^{-2}.min^{-1}, b) Simulated Bode plot and experimental one after correction with the CE at OCV, at 750°C, pH_2/pH_2O=0.1/0.9 and 6 Nml.cm^{-2}.min^{-1}.

The multiscale model has been used to calculate the local current densities at 750°C along the cell radius in the same conditions than the durability experiment (cf. section 3.1). Due to the steam consumption and the hydrogen production, the local current density decreases continuously from the cell inlet to the outlet [33] (Fig. 8a). It is equal to -1 A.cm^{-2} at a radial position of 1.2 cm from the cell center (inlet). This position corresponds to a gas composition of pH_2/pH_2O=0.54/0.46 taken at the interface between the active layer and the cermet support. For a sake of simplicity and comparison with the SOFC mode, the local overpotentials calculated in these conditions were not used to estimate the gradients of wettability but they were calculated at -1 A.cm^{-2} for a typical gas composition at the top of the active layer of pH_2/pH_2O = 0.1/0.9. These cathodic overpotentials are plotted as a function of the electrode thickness in Fig. 8b and compared to the ones computed in SOFC conditions at +1 A.cm^{-2} for the same gas composition. As expected, it can be remarked that the overpotentials are higher under cathodic polarization in SOEC mode than the ones obtained under anodic polarization in SOFC mode [14]. Finally, the same simulation has been repeated for a reverse gas composition in SOFC mode of pH_2/pH_2O = 0.9/0.1 and plotted in Fig. 8c.

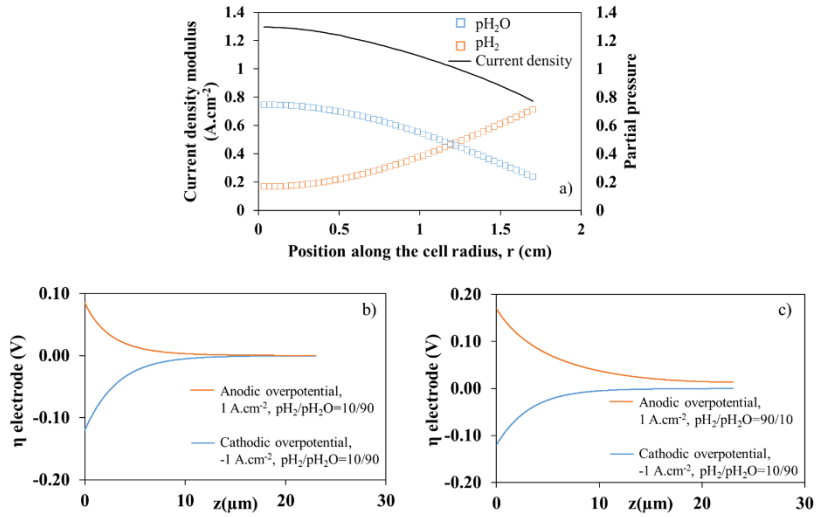

Figure 8: a) Distribution of the current density and the pH_2 and pH_2O along the cell radius r b) Cathodic and anodic overpotentials in the electrode thickness at 750°C, -/+1 A.cm^{-2}, pH2/pH_2O = 0.1/0.9 and 6 Nml.cm^{-2}.min^{-1} c) Cathodic and anodic overpotentials in the electrode thickness at 750°C, -/+1 A.cm^{-2}, pH_2/pH_2O = 0.1/0.9 pH_2/pH_2O = 0.9/0.1 respectively and 6 Nml.cm^{-2}.min^{-1}.

4.2.2 Estimation of the gradients in contact angles – The gradients of contact angles used for the phase-field simulations were calculated at +/− 1 A.cm^{-2} in SOFC and SOEC modes for a gas composition of pH_2/pH_2O = 0.9/0.1 and pH_2/pH_2O = 0.1/0.9, respectively. For this purpose, the concentrations of oxygen vacancies in the double layer at the Ni/YSZ interface have been calculated with eq. (7) using the local overpotentials given in Fig. 8c. Their profiles across the electrode thickness are plotted in Fig. 9a. As expected, a strong accumulation is found under cathodic polarization with respect to the vacancies concentration in the YSZ bulk. In contrast, only a slight depletion is observed under anodic polarization. To relate the impact of these evolutions to the Ni wettability onto YSZ, it has been assumed that the Ni is detached from YSZ when the concentration of vacancies in the double layer reaches $C_{V\ddot{o}}^{max}$. This condition, $C_{V\ddot{o}}^{int} = C_{V\ddot{o}}^{max}$, means that all the oxygen atoms have been removed from the electrolyte interface, and hence, the contact angle $\theta_{Ni/YSZ}$ is equal to $\theta_{Ni/YSZ}^{max} = 180°$. At equilibrium when the concentration of vacancies is equal to $C_{V\ddot{o}}^{int} = C_{V\ddot{o}}^{bulk}$, the contact angle $\theta_{Ni/YSZ}^{eq}$ can be expressed as a function of the local oxygen partial pressure as follows [51] :

$$\theta_{Ni/YSZ}^{eq} = \cos^{-1}\left(\frac{W_{adh}}{\gamma^{p} - \Gamma_O RT\ln\left(1 + K_a\left(2.38\times10^{-4}\left(\frac{p_{O_2}^{eq}}{p}\right)^{0.5}\exp\left(\frac{1.82\times10^{5}}{RT}\right)\right)\right)} - 1\right) \quad (10)$$

where W_{adh} is the work of adhesion at the Ni/YSZ interface, γ^p the surface tension of pure Ni without oxygen adsorption, Γ_O is the saturation coverage of oxygen adsorption on Ni surface and K_a is the oxygen adsorption coefficient. The terms R and p denote the ideal gas constant and the atmospheric pressure. The oxygen partial pressure at equilibrium $p_{O_2}^{eq}$ has been taken at the top of the active layer layer (z = ℓ) where the overpotentials tend to zero. It has been calculated with the hydrogen and steam partial pressures assuming that the hydrogen combustion reaction at 750°C (i.e. $1/2O_2 + H_2 \leftrightarrow H_2O$) is at the thermodynamic equilibrium [52]:

$$p_{O_2}^{eq} = \left(\frac{p_{H_2O}^{eq}}{p_{H_2}^{eq}\exp\left(\frac{-\Delta G}{RT}\right)}\right)^2 \quad (11)$$

Where the variation in Gibbs energy is given by [53] :

$$\Delta G = -248300 + 55.7 \times T \ [J/mol] \quad (12)$$

The contact angles at equilibrium can be thus calculated combining eqs (10), (11) and (12) and using the input data listed in Table I. Finally, a semi-empirical approach has been adopted to express the contact angle. Indeed, it is worth noting that the contact angles under polarization have been computed as a function of the oxygen vacancies assuming a linear dependence between the two bounds $\theta_{Ni/YSZ}^{eq} = f\left(C_{V_{\ddot{O}}}^{bulk}\right)$ and $\theta_{Ni/YSZ}^{max} = f(C_{V_{\ddot{O}}}^{max})$. The evolution of the contact angles in the thickness of the electrode active layer is provided in Fig. 9b for the two operating modes. A steep decrease of the Ni/YSZ contact angles from the electrolyte interface is found in SOEC mode leading to a high gradient in wettability (≈ 27° / 23 µm). This gradient should thus trigger a substantial Ni migration away from the electrolyte interface. On the contrary, only a slight increase in the contact angle is calculated from the electrolyte interface in SOFC mode. It is associated to a low gradient in wettability (≈ -2°/ 23 µm) that should drive a slow Ni migration towards the electrolyte interface.

Table I. Data used to calculate the Ni/YSZ contact angle at equilibrium.

Parameter	Value	Ref.
W_{adh}	1.4 [J.m^{-2}]	[51]
R	8.314 [J.K^{-1}.mol^{-1}]	-
T	1023 [K]	-
Γ_O	0.41 [N.m^{-1}]	[51]
K_a	1200	[51]
γ^p	$1829 - 0.4014(T - 1728)$ [10^{-3} N.m^{-1}]	[52]

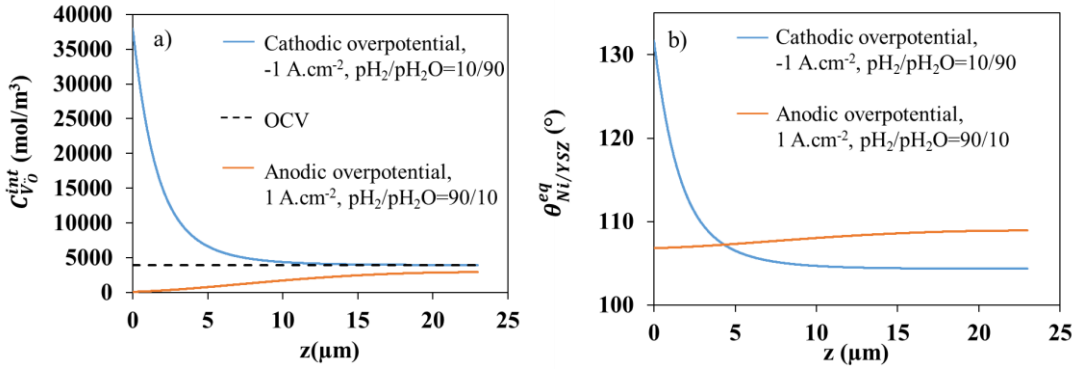

Figure 9: a) Evolution of the oxygen vacancies concentration in the electrochemical double layer (DL) as a function of the electrode thickness at OCV and for the cathodic and anodic polarization at 750°C, -/+1 A.cm^{-2}, pH_2/pH_2O = 0.1/0.9 and pH_2/pH_2O = 0.9/0.1 respectively and 6 Nml.cm^{-2}.min^{-1} b) Ni/YSZ contact angle as a function of the electrode thickness in the same conditions.

4.2.3 Migration of Ni in SOEC and SOFC modes

The phase-fields simulations were carried out for an operation of 402.8 h either at OCV or in SOFC and SOEC modes at i = +/-1 A.cm^{-2} and 750°C. The simulations at OCV were conducted with a constant Ni/YSZ contact angle taken at equilibrium to 105° [51] while the gradients reported in Fig. 9b were used for the phase-field computation in SOEC and SOFC modes. A large representative volume of the electrode microstructure of 6 × 6 × 15 µm^3, including a part of the electrolyte, was taken as initial state to well describe the local

heterogeneities especially in the electrode thickness. The phase-field simulations on such a large volume are very long and require several months of computation. Therefore, the simulations were stopped at 402 h which is a tradeoff between a reasonable computation time (5 months) and a microstructural evolution which is sufficient to highlight the migration.

The 3D microstructure of the Ni-YSZ electrode is shown in Fig. 10a for the initial state whereas the ones simulated by the phase-field model are displayed in Fig. 10b-d. For the sake of clarity, only the Ni phase is shown in these 3D rendering volumes. By their visual inspection, it is clear that the pristine microstructure contains quite some small Ni particles (Fig. 10a, highlighted by the circles), which disappear in the three simulated 3D microstructures as shown in Fig. 10b, c and d. Moreover, the Ni migration cannot be clearly observed in the 3D rendering volumes after an operation of only 402.8 h. In order to better highlight the Ni redistribution, the mass center calculated over the electrode thickness and the distribution of the phase volume fractions have been determined for the reference and the aged simulated microstructures.

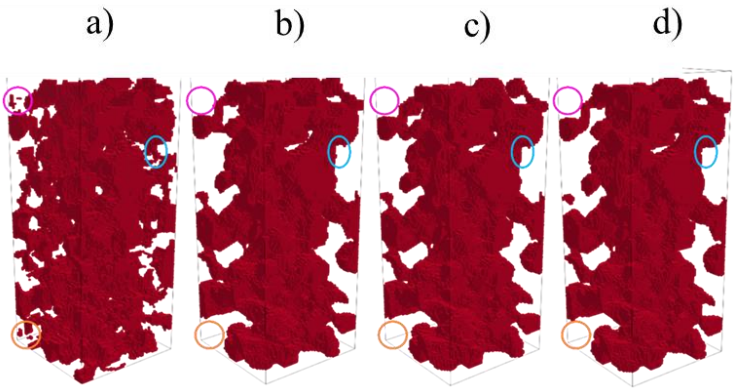

Figure 10: 3D microstructures of the Ni-YSZ electrode showing the Ni phase only for: a) initial micro structure (experimental data), b) at OCV with a contact angle of 105° for 402.8 h (simulated), c) in SOEC (-1 $A.cm^{-2}$, pH_2/pH_2O = 0.1/0.9, 6 $Nml.cm^{-2}.min^{-1}$ and 750°C) with the Ni/YSZ contact angles gradient calculated in Fig. 9b for 402.8 h (simulated), and d) in SOFC (1 $A.cm^{-2}$, pH_2/pH_2O = 0.9/0.1, 6 $Nml.cm^{-2}.min^{-1}$ and 750°C) with the Ni/YSZ contact angles gradient calculated in Fig. 9b for 402.8 h (simulated).

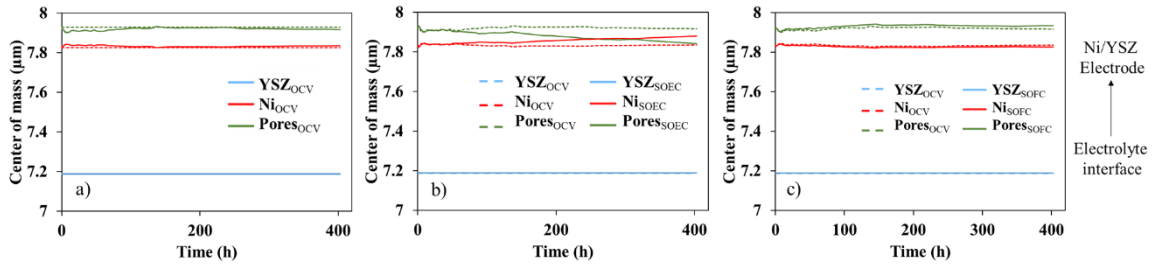

Figure 11: Evolution as a function of time of the mass center calculated over the electrode thickness for the Ni, YSZ, and pore phases for an operation at a) OCV with a contact angle of 105° and in b) SOEC (-1 A.cm^{-2}, pH_2/pH_2O = 0.1/0.9, 6 Nml.cm^{-2}.min^{-1} and 750°C) with the Ni/YSZ contact angles gradient calculated in Fig. 9b and c) SOFC (1 A.cm^{-2}, pH_2/pH_2O = 0.9/0.1, 6 Nml.cm^{-2}.min^{-1} and 750°C) with the Ni/YSZ contact angles gradient calculated in Fig. 9b. The dashed lines in a) represent the case for the reference microstructure, whereas in b) and c) represent the mass center calculated for the electrode aged at OCV.

The evolutions of the mass center for the Ni, YSZ and pore phases are plotted as a function of time in Fig. 11. For the YSZ phase, the center of mass calculated over the electrode thickness remains unchanged during operation for the three investigated cases. This statement is consistent with the assumption that the YSZ backbone does not evolve during long-term operation at 750 ^{o}C [47]. It is also in good agreement with our experimental results for which the YSZ network was found to remain unaffected by an operation of 2000 h at 750°C (cf. Fig. 5). On the other hand, it can be noticed that the center of mass for the Ni and pore phases moves differently depending on the condition of cell ageing (at OCV or in SOEC and SOFC modes). Indeed, as shown in Fig. 11a at OCV, the center of mass for both Ni and pore moves slightly compared to the initial position calculated for the reference microstructure. However, no obvious direction of mass redistribution (i.e. mass transfer towards the electrolyte or the opposite) is detected. It can be reasonably assumed that these small spatial rearrangement of the Ni phase may be driven by local inhomogeneities in the initial microstructure and the follow-up Ni coarsening.

The time evolution of the mass center for Ni and pore phases obtained during operation in SOEC mode is plotted in Fig. 11b and compared to the one calculated for an ageing at OCV. The differences between the two curves are thus independent on the Ni rearrangement induced by the inhomogeneities in the microstructure. The differences that arise between the

two curves can be thus directly ascribed to the Ni migration due to the gradient of wettability (nil for ageing at OCV and equal to the dashed curve in Fig. 11b). As shown in Fig. 11b, no difference are found in the early stage of cell operation up to around 50 h. However, beyond this time, a clear evolution of both the Ni and pore phases is observed. It is found that the Ni moves towards the top of the electrode functional layer while the pore phase follows the opposite trend with a displacement of the center of mass towards the electrolyte interface. Therefore, as expected, a noticeable Ni migration away from the electrolyte interface is calculated in our conditions after 402.8 h. This result points out that the gradient in contact angles estimated according to the proposed mechanism in SOEC mode is able to trigger a substantial Ni redistribution away from the electrolyte interface even for a relative short time of operation. Therefore, this simulation result is consistent with the post-mortem observations of the tested cell which have revealed a strong Ni depletion at the electrolyte interface for the same operating conditions at 750°C and -1 $A.cm^{-2}$.

The time evolutions of both Ni and pore mass centers in SOFC mode are compared to the ones at OCV in Fig. 11c. In this case, the curves for the Ni and pore phases are almost superimposed. Only a very slight movement of the Ni mass center is detected corresponding to a Ni enrichment at the electrolyte interface which is hardly visible. This evolution is accompanied by the opposite movement for the mass center for the porosity which tends to decrease at the electrolyte interface. Therefore, the gradient of contact angles are not able to drive a significant Ni redistribution in SOFC mode. According to these modeling results, the mechanism is able to predict a strong Ni redistribution under SOEC condition and a very slow Ni migration in SOFC mode that could be detected only after a very long-term durability experiment.

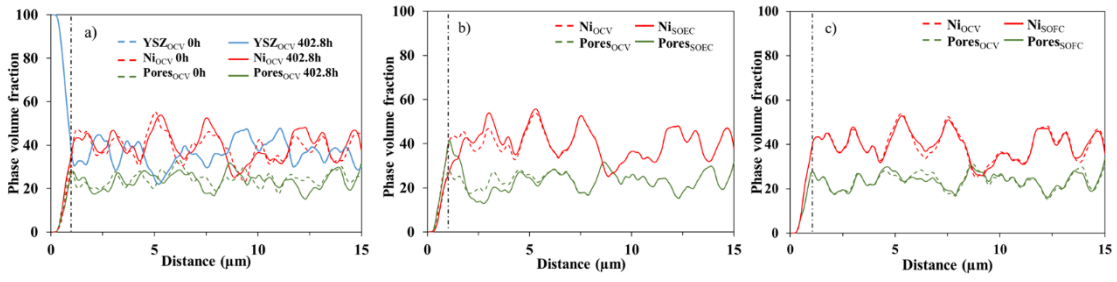

Figure 12: Phase fraction of the three phases in a) OCV with a contact angle of 105°, b) SOEC (-1 $A.cm^{-2}$, pH_2/pH_2O = 0.1/0.9, 6 $Nml.cm^{-2}.min^{-1}$ and 750°C) with the Ni/YSZ contact angles gradient calculated in Fig. 9b and c) SOFC (1 $A.cm^{-2}$, pH_2/pH_2O = 0.9/0.1, 6

Nml.cm^{-2}.min^{-1} and 750°C) with the Ni/YSZ contact angles gradient calculated in Fig. 9b (The gray dashed line marks the position for the electrolyte/electrode interface).

To go further in the analysis and to explore in details the Ni migration, the local variations of the phase volume fractions have been measured on the simulated microstructures. They are plotted in Fig. 12 as a function of the position in the electrode thickness (i.e. in the direction perpendicular to the electrolyte interface). In Fig. 12a, the curves obtained after operation at OCV are compared to the initial microstructure (at t = 0 h). As already mentioned, the phase volume fraction of YSZ remain unchanged with time, as the solid blue line overlaps with the dashed blue line entirely in Fig. 12a. Thus, the YSZ phase fraction was not analyzed further. However, the phase volume fractions of Ni and pores at OCV deviate from those calculated for the pristine microstructure. Nevertheless, there is no indication of Ni redistribution over long distances which is in good agreement with the evolution of the mass center shown in Fig. 11a. This result confirms that local rearrangements of Ni particles arises in the microstructure due the coarsening of the initial inhomogeneous microstructure. The plots obtained for the simulated microstructures in SOEC mode at t = 402.8 h is compared in Fig. 12b to the ones computed at OCV for the same time. It can be noticed that the Ni depletion zone extends from the electrolyte interface over a distance of around ≈ 2.5 µm in the functional layer. It is followed by a second region in the electrode where the cermet is enriched by the Ni coming from the depleted zone. As expected, an opposite behavior can be observed for the porosity for which a more porous layer of ≈ 2.5 µm is detected at the electrolyte interface. The extent of Ni depletion due to the migration in SOEC mode is roughly consistent with our experiments. Nevertheless, in our condition, the depleted zone was found to spread over a distance of around 4 µm (Fig. 5c). The discrepancy between the experimental and simulated results can be obviously explained since the simulations were run for a shorter time. Besides, it can be speculated that the microstructural change due to the Ni migration can affect the electrochemical response by changing the repartition of the overpotentials in the electrode thickness (since a zone close to the electrolyte interface must become inactive due to the Ni loss). From this point of view, it would be necessary to improve the model with a staggered resolution integrating both the electrochemical and phase-field simulations. In this case, the gradients of contact angles should be calculated at each time where a noticeable microstructure change is obtained with the phase-field model. Moreover, it cannot be fully excluded that Ni migration also occurs in the gas phase resulting in a higher depleted zone.

Nevertheless, Lei et al. [21] have found that the mechanism based on the $Ni(OH)_2$ gas diffusion is not sufficient to explain the Ni redistribution at 800°C.

Finally, the profiles of phase volume fractions obtained for an operation at OCV and in SOFC mode are plotted in Fig. 12c. As foreseen after a short operation in SOFC mode, there is no significant Ni redistribution in the electrode. This statement confirms that the Ni enrichment can be observed only after a very long-term durability experiment. This behavior is due to the small gradient in the Ni/YSZ contact angle calculated in SOFC mode.

According to the phase-field model, Ni migrates from high to low contact angles in both SOEC and SOFC modes. Indeed, the rate of migration depends on the contact angle gradient, which means that higher contact angle gradient can cause a more significant Ni migration. Thanks to the proposed mechanism, a relative high gradient in Ni wettability was calculated that is able to drive a significant Ni depletion in electrolysis mode. On the contrary, the gradient of contact angles estimated in SOFC mode was found to be insufficient to trigger a noticeable Ni redistribution.

Regarding typical porous electrodes, it appears that the mechanism is consistent with our experimental results and most of the ones reported in literature [14] [15] [16] [17]. Indeed, for cells operated in SOEC mode below 900°C, a large Ni depletion is usually observed at the electrolyte interface [14]. However, a reverse behavior has been observed at 950°C with a Ni relocation at the electrolyte interface. In this particular condition, it has been suggested that Ni can be transported in the gas phase with a Ni accumulation at the electrolyte interface [5]. On the other hand, in SOFC mode, no significant Ni redistribution is observed after operation. For instance, using the same type of cermet, Trini et al. [14] have detected a Ni migration only in SOEC mode and not under SOFC polarization. Nonetheless, few authors have found a Ni enrichment at the electrode interface after SOFC operation. Menzler et al. [16] have detected a slight Ni migration toward the electrolyte after an operation of 100,000 h. This microstructural evolution could be still compatible with the low wettability gradient estimated in this work. However, Parikh [54] observed a substantial Ni enrichment for an operation at 800°C, 860°C and 925°C after 8000 h. In this case, the low wettability gradients calculated with the model could failed to explain this experimental result. Nevertheless, it would be very interesting to compute the actual extension of the depleted zone in order to state the extent to which the model can reproduce these experiments.

Regarding patterned nickel-film electrode, Jiao et al. observed a Ni detachment in SOEC mode, which is consistent with the interface weakening due to the accumulation of oxygen vacancies in the double layer. Under fuel cell polarization, they observed a higher wettability of Ni onto YSZ. Even though this evolution is coherent with the change of Ni/YSZ interface energy due to the change in oxygen vacancy concentration, it is expected to be very limited in our case. Therefore, it could be explained by another modification of the Ni/YSZ interface, which remains nowadays unclear (segregation of impurities, etc…). In other words, the change of the Ni/YSZ interfacial energy, which has been attributed to a modification of the electrochemical double layer, could be also induced by other physicochemical processes controlled by the electrode polarization.

Aside from the mechanism based on wettability gradient, it has been proposed in [20] that the detached Ni particles, which are no longer polarized, could migrate via $Ni(OH)_x$ surface or gas species depending on the temperature. This mechanism is well consistent with the experiment of Jiao et al. [55]. However, as pointed out by Lei et al. [29] this hypothesis 'is unlikely to explain those experiments in fuel cell mode which report Ni enrichment near the electrolyte layer' as it 'relies on a significant loss of contact between Ni particles and between Ni and YSZ'. Moreover, this mechanism does not explain the Ni migration observed under dry CO_2 analysis [56] [57]. Therefore, it can be suspected that both mechanisms could coexist in order to explain all the experiments results. One of the two could become predominant depending on the operating conditions, the cermet microstructure and/or the properties of the Ni/YSZ interface (e.g. interfacial energy depending on impurities at interface).

From this discussion, it appears that the underlying mechanisms for Ni migration are complex and involve several processes depending on the experimental conditions or tested cermet. Even if our modeling results seem consistent with most of the experimental results conducted on porous cermet, further simulations, experiments and post-test characterizations are still required to validate the mechanism proposed in this article. Therefore, it is clear that additional investigations are still needed to clarify the mechanism of Ni migration by taking into consideration other phenomena such as the segregation of impurities under polarization.

5. Conclusion

In this work, a mechanism to account for the Ni migration in the Ni/YSZ electrode has been proposed. It is based on the impact of the electrode overpotential and the oxygen vacancies in

the electrochemical double layer on the Ni wettability onto YSZ. This mechanism yields gradients in Ni/YSZ contact angles that drive a Ni migration from low wettability to high wettability regions (i.e. from high to low Ni/YSZ contact angles).

To illustrate the Ni migration in Ni-YSZ cermet, a long-term-test of 2000 h has been carried out in electrolysis mode using a typical cell. The test has been performed at 750°C and high current density (i.e. -1 $A.cm^{-2}$, pH_2/pH_2O = 0.1/0.9 and SC = 64%). Observations of the operated cell have been conducted on polished cross-sections with a high-resolution SEM. The post-mortem characterizations on the aged cell have revealed significant Ni depletion over a distance of ≈ 4 µm from the electrolyte interface. In order to confirm these results, the cermet microstructures of the pristine and the aged cells have been reconstructed by FIB-SEM tomography. The evolution of the cermet microstructural properties have been measured on the reconstructed volumes. The microstructural analyses have highlighted the decrease of the Ni phase volume fraction at the electrolyte interface as well as the active TPB density in this same region confirming the Ni migration.

In order to assess the relevance of the proposed mechanism, a numerical model has been built coupling a multi-scale electrochemical model with phase-field simulations. The electrochemical model has been used to assess the local electrode overpotentials in the electrode thickness and to calculate the gradient of Ni/YSZ contact angles in the same condition than the experiments (i.e. in SOEC mode at -1 $A.cm^{-2}$, 750°C, pH_2/pH_2O = 0.1/0.9). These gradients together with the reconstruction of the pristine electrode were used as input data in the phase-field model. The simulations have shown that a substantial Ni depletion occurs after an operation of 402.8 h. Moreover, the simulated depleted zone has been found in the same range of magnitude than the experimental one (albeit lower). To complement the modeling results, simulations have been performed in reverse conditions at +1 $A.cm^{-2}$ in SOFC mode (750°C, pH_2/pH_2O = 0.9/0.1). In this case, only a negligible Ni redistribution with a very slight Ni enrichment at the electrolyte interface has been found. The simulations based on the implemented mechanism are thus consistent with the observations of the tested cell in SOEC mode. They are also coherent with the experimental studies which have reported a substantial Ni depletion in SOEC mode and a very moderate enrichment in SOFC mode. However, the mechanism failed to reproduce all the experimental results reported in the literature. From, this point of view, further experimental and modeling investigations are still

required to better understand the complex underlying mechanism controlling the Ni migration.

Acknowledgements

This project has received funding from the Fuel Cells and Hydrogen 2 Joint Undertaking (Ju under grand agreement n°874577 (NewSOC project). The work has also been supported by Genvia and the project CELCER-EHT and EP2Gas (EUDP project no. 64017-0011 Efficient Power2Gas combining SOEC and Biomass Gasification).

References

[1] E. L. V. Eriksson and E. MacA. Gray, 'Optimization and integration of hybrid renewable energy hydrogen fuel cell energy systems – A critical review', Appl. Energy, vol. 202, pp. 348–364, (2017), doi: 10.1016/j.apenergy.2017.03.132.

[2] Q. Cai, C. S. Adjiman, and N. P. Brandon, 'Optimal control strategies for hydrogen production when coupling solid oxide electrolysers with intermittent renewable energies', J. Power Sources, vol. 268, pp. 212–224, (2014), doi: 10.1016/j.jpowsour.2014.06.028.

[3] A. Godula-Jopek, Hydrogen Production: by Electrolysis, P.191, John Wiley & Sons, (2015).

[4] L. Blum, U. Packbier, I. C. Vinke, and L. G. J. de Haart, 'Long-Term Testing of SOFC Stacks at Forschungszentrum Jülich', Fuel Cells, vol. 13, no. 4, pp. 646–653, (2013), doi: 10.1002/fuce.201200151.

[5] A. Hauch, S. D. Ebbesen, S. H. Jensen, and M. Mogensen, 'Solid Oxide Electrolysis Cells: Microstructure and Degradation of the Ni/Yttria-Stabilized Zirconia Electrode', J. Electrochem. Soc., vol. 155, no. 11, p. B1184, (2008), doi: 10.1149/1.2967331.

[6] T. L. Skafte, J. Hjelm, P. Blennow, and C. Graves, 'Quantitative review of degradation and lifetime of solid oxide cells and stacks', Proceedings of 12th European SOFC & SOE Forum, Lucerne, Switzerland, (2016).

[7] D. Papurello, A. Lanzini, S. Fiorilli, F. Smeacetto, R. Singh, and M. Santarelli, 'Sulfur poisoning in Ni-anode solid oxide fuel cells (SOFCs): Deactivation in single cells and a stack', Chem. Eng. J., vol. 283, pp. 1224–1233, (2016), doi: 10.1016/j.cej.2015.08.091.

[8] H. Madi, A. Lanzini, S. Diethelm, D. Papurello, J. Van herle, M. Lualdi, J. Gutzon Larsen and M. Santarelli, 'Solid oxide fuel cell anode degradation by the effect of siloxanes', J. Power Sources, vol. 279, pp. 460–471, (2015), doi: 10.1016/j.jpowsour.2015.01.053.

[9] K. Chen and S. P. Jiang, 'Review—Materials Degradation of Solid Oxide Electrolysis Cells', J. Electrochem. Soc., vol. 163, no. 11, pp. F3070–F3083, (2016), doi: 10.1149/2.0101611jes.

[10] H. Yokokawa, H. Tu, B. Iwanschitz, and A. Mai, 'Fundamental mechanisms limiting solid oxide fuel cell durability', J. Power Sources, vol. 182, no. 2, pp. 400–412, (2008), doi: 10.1016/j.jpowsour.2008.02.016.

[11] R. VAßEN and D. Simwonis, 'Modelling of the agglomeration of Ni-particles in anodes of solid oxide fuel cells', J. Mater. Sci. 36, (1), 147-151, (2001).

[12] M. Hubert, J. Laurencin, P. Cloetens, B. Morel, D. Montinaro, and F. Lefebvre-Joud, 'Impact of Nickel agglomeration on Solid Oxide Cell operated in fuel cell and electrolysis modes', J. Power Sources, vol. 397, pp. 240–251, (2018), doi: 10.1016/j.jpowsour.2018.06.097.

[13] M. B. Mogensen, A. Hauch, X. Sun, M. Chen, Y. Tao, S. Ebbesen, K. Hansen and P. Hendriksen, 'Relation Between Ni Particle Shape Change and Ni Migration in Ni-YSZ

Electrodes - a Hypothesis', Fuel Cells, vol. 17, no. 4, pp. 434–441, (2017), doi: 10.1002/fuce.201600222.
[14] M. Trini, A. Hauch, S. De Angelis, X. Tong, P. V. Hendriksen, and M. Chen, 'Comparison of microstructural evolution of fuel electrodes in solid oxide fuel cells and electrolysis cells', J. Power Sources, vol. 450, p. 227599, (2020), doi: 10.1016/j.jpowsour.2019.227599.
[15] F. Monaco, M. Hubert, J. Vulliet, J.P. Ouweltjes, D. Montinaro, P. Cloetens, P. Piccardo, F. Lefebvre-Joud and J. Laurencin, 'Degradation of Ni-YSZ Electrodes in Solid Oxide Cells: Impact of Polarization and Initial Microstructure on the Ni Evolution', J. Electrochem. Soc., vol. 166, no. 15, pp. F1229–F1242, (2019), doi: 10.1149/2.1261915jes.
[16] N. H. Menzler, D. Sebold, Y. J. Sohn, and S. Zischke, 'Post-test characterization of a solid oxide fuel cell after more than 10 years of stack testing', J. Power Sources, vol. 478, p. 228770, (2020), doi: 10.1016/j.jpowsour.2020.228770.
[17] M. Chen, Y. Liu, J. J. Bentzen, W. Zhang, X. Sun, A. Hauch, Y. Tao, J. R. Bowen and P. V. Hendriksen, 'Microstructural Degradation of Ni/YSZ Electrodes in Solid Oxide Electrolysis Cells under High Current', J. Electrochem. Soc., vol. 160, no. 8, pp. F883–F891, (2013), doi: 10.1149/2.098308jes.
[18] A. Hauch, K. Brodersen, M. Chen, and M. B. Mogensen, 'Ni/YSZ electrodes structures optimized for increased electrolysis performance and durability', Solid State Ion., vol. 293, pp. 27–36, (2016), doi: 10.1016/j.ssi.2016.06.003.
[19] A. Sciazko, T. Shimura, Y. Komatsu, and N. Shikazono, 'Ni-GDC and Ni-YSZ electrodes operated in solid oxide electrolysis and fuel cell modes', J. Therm. Sci. Technol., vol. 16, no. 1, pp. JTST0013–JTST0013, (2021), doi: 10.1299/jtst.2021jtst0013.
[20] M. B. Mogensen, M. Chen, H. L. Frandsen, C. Graves, A. Hauch, P. V. Hendriksen, T. Jacobsen, S. H. Jensen, T. L. Skafte and X. Sun, 'Ni migration in solid oxide cell electrodes: Review and revised hypothesis', Fuel Cells, p. fuce.202100072, (2021), doi: 10.1002/fuce.202100072.
[21] Y. Lei, W. Epting, J. Masson, T. Cheng, H. Abernathy, G. Hackett and Y. Wen, 'Simulating Microstructure Evolution in Ni-YSZ Electrodes of Solid Oxide Cells Under Operating Conditions', in TMS 2022 151st Annual Meeting & Exhibition Supplemental Proceedings, The Minerals, Metals & Materials Society, Ed. Cham: Springer International Publishing, pp. 457–469, (2022),. doi: 10.1007/978-3-030-92381-5_42.
[22] A. Nakajo, G. Rinaldi, P. Caliandro, G. Jeanmonod, L. Navratilova, M. Cantoni and J. Van herle 'Evolution of the Morphology Near Triple-Phase Boundaries in Ni–Yttria Stabilized Zirconia Electrodes Upon Cathodic Polarization', J. Electrochem. Energy Convers. Storage, vol. 17, no. 4, p. 041004, (2020), doi: 10.1115/1.4046478.
[23] D. C. Grahame, 'The Electrical Double Layer and the Theory of Electrocapillarity.', Chem. Rev., vol. 41, no. 3, pp. 441–501, (1947), doi: 10.1021/cr60130a002.
[24] S. Gao, J. Li, and Z. Lin, 'Theoretical model for surface diffusion driven Ni-particle agglomeration in anode of solid oxide fuel cell', J. Power Sources, vol. 255, pp. 144–150, (2014), doi: 10.1016/j.jpowsour.2014.01.033.
[25] H.-Y. Chen, 'Simulation of coarsening in three-phase solid oxide fuel cell anodes', J. Power Sources, p. 5, (2011).
[26] M. Trini, S. De Angelis, P. S. Jørgensen, P. V. Hendriksen, K. Thornton, and M. Chen, 'Towards the Validation of a Phase Field Model for Ni Coarsening in Solid Oxide Cells', Acta Mater., p. 116887, (2021), doi: 10.1016/j.actamat.2021.116887.
[27] Y. Wang, C. Wu, Q. Du, M. Ni, K. Jiao, and B. Zu, 'Morphology and performance evolution of anode microstructure in solid oxide fuel cell: A model-based quantitative analysis', Appl. Energy Combust. Sci., vol. 5, p. 100016, (2021), doi: 10.1016/j.jaecs.2020.100016.
[28] Y. Wang, C. Wu, B. Zu, M. Han, Q. Du, M. Ni and K. Jiao 'Ni migration of Ni-YSZ electrode in solid oxide electrolysis cell: An integrated model study', J. Power Sources, vol. 516, p. 230660, (2021), doi: 10.1016/j.jpowsour.2021.230660.
[29] Y. Lei, Y. Lee, W. Epting, J. Mason, T. Cheng, H. Abernathy, G. Hackett and Y. Wen 'Modeling Ni redistribution in the hydrogen electrode of solid oxide cells through Ni(OH)2 diffusion and Ni-YSZ wettability change', J. Power Sources, vol. 545, p. 231924, (2022), doi: 10.1016/j.jpowsour.2022.231924.

[30] F. Monaco, E. Effori, M. Hubert, E. Siebert, G. Geneste, B. Morel, E. Djurado, D. Montinaro and J. Laurencin, 'Electrode kinetics of porous Ni-3YSZ cermet operated in fuel cell and electrolysis modes for solid oxide cell application', Electrochimica Acta, vol. 389, p. 138765, (2021), doi: 10.1016/j.electacta.2021.138765.
[31] S. Berg, D. Kutra, T. Kroeger, C. N. Straehle; B. X. Kausler, C. Haubold, M. Schiegg, J. Ales, T. Beier, M. Rudy, K. Eren, J. Cervantes. B. Xu, F. Beuttenmueller, A. Wolny, C. Zhang, U. Koethe, F. A. Hamprecht and A. Kreshuk, 'ilastik: interactive machine learning for (bio)image analysis', Nat. Methods, vol. 16, no. 12, pp. 1226–1232, (2019), doi: 10.1038/s41592-019-0582-9.
[32] C. Sommer, C. Straehle, U. Köthe, and F. A. Hamprecht, 'Ilastik: Interactive learning and segmentation toolkit', in 2011 IEEE International Symposium on Biomedical Imaging: From Nano to Macro, pp. 230–233, (2011). doi: 10.1109/ISBI.2011.5872394.
[33] E. Da Rosa Silva, M. Hubert, B. Morel, H. Moussaoui, J. Debayle, and J. Laurencin, 'A Dynamic Multi-Scale Model for Solid Oxide Cells Validated on Local Current Measurements: Impact of Global Cell Operation on the Electrodes Reaction Mechanisms', ECS Trans., vol. 103, no. 1, pp. 893–907, (2021), doi: 10.1149/10301.0893ecst.
[34] E. Effori, J. Laurencin, E. Da Rosa Silva, M. Hubert, T. David, M. Petitjean, G. Geneste, L. Dessemond and E. Siebert, 'An Elementary Kinetic Model for the LSCF and LSCF-CGO Electrodes of Solid Oxide Cells: Impact of Operating Conditions and Degradation on the Electrode Response', J. Electrochem. Soc., vol. 168, no. 4, p. 044520, (2021), doi: 10.1149/1945-7111/abf40a.
[35] I. Steinbach, F. Pezzolla, B. Nestler, M. Seeßelberg, R. Prieler, G.J. Schimtz and J.L.L. Rezende, 'A phase field concept for multiphase systems', Phys. Nonlinear Phenom., vol. 94, no. 3, pp. 135–147, (1996), doi: 10.1016/0167-2789(95)00298-7.
[36] I. Steinbach and F. Pezzolla, 'A generalized field method for multiphase transformations using interface fields', Phys. Nonlinear Phenom., vol. 134, no. 4, pp. 385–393, (1999), doi: 10.1016/S0167-2789(99)00129-3.
[37] I. Steinbach, 'Phase-field models in materials science', Model. Simul. Mater. Sci. Eng., vol. 17, no. 7, p. 073001, (2009), doi: 10.1088/0965-0393/17/7/073001.
[38] J. Eiken, B. Böttger, and I. Steinbach, 'Multiphase-field approach for multicomponent alloys with extrapolation scheme for numerical application', Phys. Rev. E, vol. 73, no. 6, p. 066122, (2006), doi: 10.1103/PhysRevE.73.066122.
[39] K. Wu, 'Computer simulation of interdiffusion microstructures in multi-component and multiphase systems', The Ohio State University, (2004).
[40] M. Kilo, 'Modeling of cation diffusion in oxygen ion conductors using molecular dynamics', Solid State Ion., vol. 175, no. 1–4, pp. 823–827, (2004), doi: 10.1016/j.ssi.2004.09.059.
[41] S. Yang, J. Gao, M. Trini, S.D. Angelis, P.S. Jørgensen, J.R. Bowen, L. Zhang, M. Chen, 'Ni coarsening in Ni-yttria stabilized zirconia electrodes: Three-dimensional quantitative phase-field simulations supported by ex-situ ptychographic nano-tomography', Acta Mater., vol. 246, p. 118708, (2023), doi: 10.1016/j.actamat.2023.118708.
[42] B. Liu, H. Muroyama, T. Matsui, K. Tomida, T. Kabata, and K. Eguchi, 'Analysis of Impedance Spectra for Segmented-in-Series Tubular Solid Oxide Fuel Cells', J. Electrochem. Soc., vol. 157, no. 12, p. B1858, (2010), doi: 10.1149/1.3494214.
[43] A. Nechache, A. Mansuy, M. Petitjean, J. Mougin, F. Mauvy, B. A. Boukamp, M. Cassir and A. Ringuedé, 'Diagnosis of a cathode-supported solid oxide electrolysis cell by electrochemical impedance spectroscopy', Electrochimica Acta, vol. 210, pp. 596–605, (2016), doi: 10.1016/j.electacta.2016.05.014.
[44] G. Corre and A. Brisse, '9000 Hours Operation of a 25 Solid Oxide Cells Stack in Steam Electrolysis Mode', ECS Trans., vol. 68, no. 1, pp. 3481–3490, (2015), doi: 10.1149/06801.3481ecst.
[45] J. Villanova, J. Laurencin, P. Cloetens, P. Bleuet, G. Delette, H. Suhonen, F. Usseglio-Viretta, '3D phase mapping of solid oxide fuel cell YSZ/Ni cermet at the nanoscale by holographic X-ray nanotomography', J. Power Sources, vol. 243, pp. 841–849, (2013), doi: 10.1016/j.jpowsour.2013.06.069.

[46] F. Usseglio-Viretta, J. Laurencin, G. Delette, J. Villanova, P. Cloetens, and D. Leguillon, ‘Quantitative microstructure characterization of a Ni–YSZ bi-layer coupled with simulated electrode polarisation’, J. Power Sources, vol. 256, pp. 394–403, (2014), doi: 10.1016/j.jpowsour.2014.01.094.
[47] M. Trini, P. S. Jørgensen, A. Hauch, M. Chen, and P. V. Hendriksen, ‘Microstructural Characterization of Ni/YSZ Electrodes in a Solid Oxide Electrolysis Stack Tested for 9000 Hours’, ECS Trans., vol. 78, no. 1, pp. 3049–3064, (2017), doi: 10.1149/07801.3049ecst.
[48] M. G. H. M. Hendriks, J. E. ten Elshof, H. J. M. Bouwmeester, and H. Verweij, ‘The defect structure of the double layer in yttria-stabilised zirconia’, Solid State Ion., vol. 154–155, pp. 467–472, (2002), doi: 10.1016/S0167-2738(02)00484-8.
[49] O. A. Marina, L. R. Pederson, M. C. Williams, G. W. Coffey, K. D. Meinhardt, C. D. Nguyen and E. C. Thomsen, ‘Electrode Performance in Reversible Solid Oxide Fuel Cells’, J. Electrochem. Soc., vol. 154, no. 5, p. B452, (2007), doi: 10.1149/1.2710209.
[50] T. Sasaki, K. Matsunaga, H. Ohta, H. Hosono, T. Yamamoto, and Y. Ikuhara, ‘Atomic and Electronic Structures of Ni/YSZ(111) Interface’, Mater. Trans., vol. 45, no. 7, pp. 2137–2143, (2004), doi: 10.2320/matertrans.45.2137.
[51] Z. Jiao and N. Shikazono, ‘Study on the effects of polarization on local morphological change of nickel at active three-phase-boundary using patterned nickel-film electrode in solid oxide fuel cell anode’, Acta Mater., vol. 135, pp. 124–131, (2017), doi: 10.1016/j.actamat.2017.05.051.
[52] S. Ozawa, S. Takahashi, N. Watanabe, and H. Fukuyama, ‘Influence of Oxygen Adsorption on Surface Tension of Molten Nickel Measured Under Reducing Gas Atmosphere’, Int. J. Thermophys., vol. 35, no. 9–10, pp. 1705–1711, (2014), doi: 10.1007/s10765-014-1674-5.
[53] L. Bernadet, ‘Étude de l’effet de la pression sur l’électrolyse de H2O et la co-électrolyse de H2O et CO2 à haute température’, Université de Bordeaux, (2016).
[54] H. Parikh, ‘MICROSTRUCTURE CHANGES IN SOLID OXIDE FUEL CELL ANODES AFTER OPERATION, OBSERVED USING THREE-DIMENSIONAL RECONSTRUCTION AND MICROCHEMICAL ANALYSIS’, Case Western Reserve University, (2015).
[55] Z. Jiao, E. P. Busso, and N. Shikazono, ‘Influence of Polarization on the Morphological Changes of Nickel in Fuel Electrodes of Solid Oxide Cells’, J. Electrochem. Soc., vol. 167, no. 2, p. 024516, (2020), doi: 10.1149/1945-7111/ab6f5b.
[56] S. Jensen, A. Hauch, X. Sun, M. Chen, S. Ebbesen, M. B. Mogensen, 'Diffusion rates of reactants and components in solid oxide cells', Proc. 13th European SOFC & SOE Forum, Lucerne, Switzerland, (2018), B1208.
[57] M. Yu, X. Sun, Y. Liu, Y. Shang, M. Chen, Electrochemical performance of solid oxide cells operated in CO2 electrolysis, 15th European SOFC & SOE Forum, Lucerne, (2022), B09s12, p.893.